JARS Journal of Applied Remote Sensing

RESEARCH PAPER

Evaluation of Doppler wind lidar for advanced air mobility

Adam Medina,[a,b,*] Zackary Mitchell,[a] Tyler Willhite,[a] Jeremy W. Hopwood,[c] Charvi Pande,[a] Stephan F. J. De Wekker,[d] Craig Woolsey,[c] Kyle Renshaw,[b] and Grady J. Koch[a]

[a]NASA Langley Research Center, Hampton, Virginia, United States
[b]University of Central Florida, The College of Optics and Photonics, Knight Vision Lab, Orlando, Florida, United States
[c]Virginia Tech, Department of Aerospace and Ocean Engineering, Blacksburg, Virginia, United States
[d]University of Virginia, Department of Environmental Sciences, Charlottesville, Virginia, United States

ABSTRACT. Understanding wind conditions is critical for the NASA Advanced Air Mobility (AAM) mission. The types of aircraft, and the region of the atmosphere they operate in, make them highly susceptible to wind effects. We demonstrate the feasibility of using wind lidar to measure wind dynamics for the AAM mission. Wind vector measurements from two Doppler wind lidars using dual-Doppler techniques are compared with *in situ* measurements from a ground-based sonic anemometer and small uninhabited aircraft systems (sUAS). Both lidar beams intersected directly above a sonic anemometer and measurements were compared. The resulting root mean square error values between the two instruments' speed and direction measurements were 1.72 m/s and 23.05 deg, respectively. Following this test, a dual-Doppler scan pattern which measured wind vectors along a vertical column was performed while a sUAS measured wind vectors along the scanned volume for comparison. The wind profiles from the two measurement techniques are consistent and demonstrate the potential of using Doppler lidar for AAM.

Keywords: lidar; dual-Doppler; wind; remote sensing; drones; UAS; small uninhabited aircraft systems

Paper 240380G received Jun. 17, 2024; revised Dec. 3, 2024; accepted Dec. 16, 2024; published Jan. 8, 2025.

1 Introduction

The aviation community has envisioned a new air transportation system, called Advanced Air Mobility (AAM) by NASA, that involves the low-altitude operation of a new class of air vehicles.[1,2] The low altitudes of the envisioned flight paths would have these vehicles spending most of their operation in conditions where unpredictable wind and turbulence effects may occur. Such wind conditions are associated with the complex dynamics of the atmospheric boundary layer (ABL),[3] flight operations close to building structures,[4] terrain effects from flying at low altitudes, or wake turbulence effects from many vehicles operating from the same "vertiport" take-off/landing zone.[5,6] Wind measurements will hence be critical to ensure safe and efficient operations for AAM. Such wind measurement could be used as a monitoring system for warning of hazardous wind events,[7] as data input to forecasting models, or as a research tool to understand wind effects in complex environments. Requirements for wind sensing in the AAM application are anticipated to include:

*Address all correspondence to Adam Medina, adam.a.medina@nasa.gov

- Measurements ranging from near ground to 100 s of meters in altitude
- Wind vector resolution 1 m/s or better in speed and 10 deg or better in direction
- Spatial resolution of <10 m
- Sufficient sampling frequency to capture wind variations, such as profiling to 100-m height in < 1 min
- Near real-time output of measurement results
- Operations free from safety hazards (such as eye safety from laser exposure)
- All-weather capability
- Minimal footprint to not obstruct flight operations

Doppler lidar is a leading candidate for these possible requirements, as shown by its decades-long history of being an effective tool for many wind studies.[5–21] However, there is a need to re-assess the Doppler wind lidars for the AAM application which involves evaluating wind effects as vehicles operate in and out of vertiports, notably regarding spatial resolution. The capability of Doppler wind lidars to collect wind data at varying spatial resolutions using different scanning techniques, whether employing a single lidar or multiple systems, has been previously demonstrated.[5–21] Meeting the needs for AAM spatial resolution may involve the use of multiple Doppler wind lidars, which are investigated in this study. The goal of this study is to demonstrate and evaluate Doppler wind lidar capabilities for AAM applications.

The study was furthermore motivated by looking toward the future of AAM, in which the air vehicles involved can also provide wind measurements.[21–35] Airborne wind measurements, obtained directly from vehicle-mounted anemometers or indirectly from vehicle navigation data, offer a means to compare remotely sensed wind lidar with *in situ* measurements. The following sections report comparisons of wind measurements obtained using lidar and the small uninhabited aircraft systems (sUAS's) operating in the same volume of air.

2 Methodology

A field test was designed to co-locate wind lidars with *in situ* anemometers. Although the ultimate AAM application will likely involve complex urban geometry, this first test was conducted in an open area, free of as much wind complexity as possible. Once instrument performance in simple conditions is tested, a future step would be the installation of lidars close to large building structures. For this first test in an open area, Kentland Experimental Aerial Systems (KEAS) facility was selected. KEAS is located on more than 1800 acres of farmland owned and operated by the Virginia Polytechnic Institute and State University (Virginia Tech) within Montgomery County, Virginia (Fig. 1).

This facility also includes a small airstrip to support research on sUAS flight dynamics and operations. Featured instrumentation were two commercial Doppler wind lidars, which are shown in Fig. 2.

These lidars were similar models from the same manufacturers, though with some differences in software control features. Lidar 1 [Fig. 2(a)] belongs to NASA Langley Research Center and was placed freestanding, on a concrete pad located at (Lat: 37.196332 deg Lon: −80.578482 deg). The second lidar [Fig. 2(b)] belongs to the University of Virginia (UVA) and was positioned in a mobile trailer (Lat: 37.1970934 deg, Lon: −80.5790255 deg) with the beam steering optics mounted through the roof of the trailer. The relative placement of these lidars is indicated in Fig. 1. Alignment and calibration of the scan angle from each lidar were made to a surveyed reference point (Lat: 37.196916 deg, Lon: −80.578435 deg) at one end of the KEAS airstrip (see Fig. 1).

Beginning on September 13, 2022, lidar 1 would perform single lidar Velocity Azimuth Display (VAD) scans which measure range resolved horizontal wind speed and direction over the sampled volume. During the single-lidar VAD scans, a Virginia Tech pilot operated a custom sUAS within the lidar-sampled air volume and measured wind speed and direction derived from vehicular sensors and a dynamic vehicle model described in Refs. 22–31. Details of all flights and lidar scan patterns are further discussed in Section 4.1.

Following the single-Doppler VAD scans from lidar 1, dual-Doppler lidar scans began with the deployment of lidar 2 on November 7, 2022. These dual-Doppler scans allowed for direct

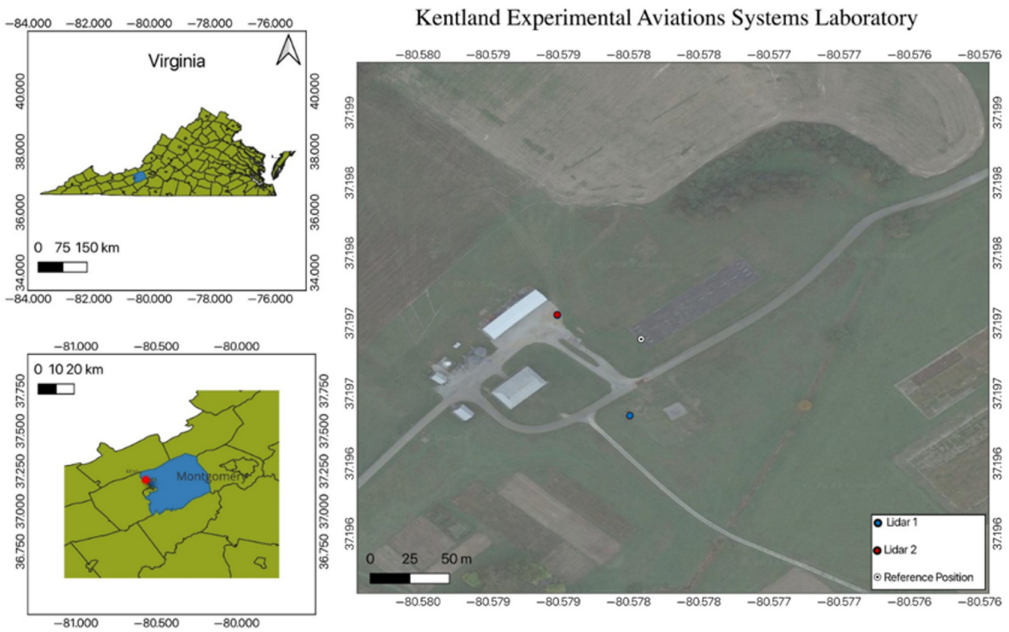

Fig. 1 Location of KEAS Laboratory and Doppler wind lidar units.

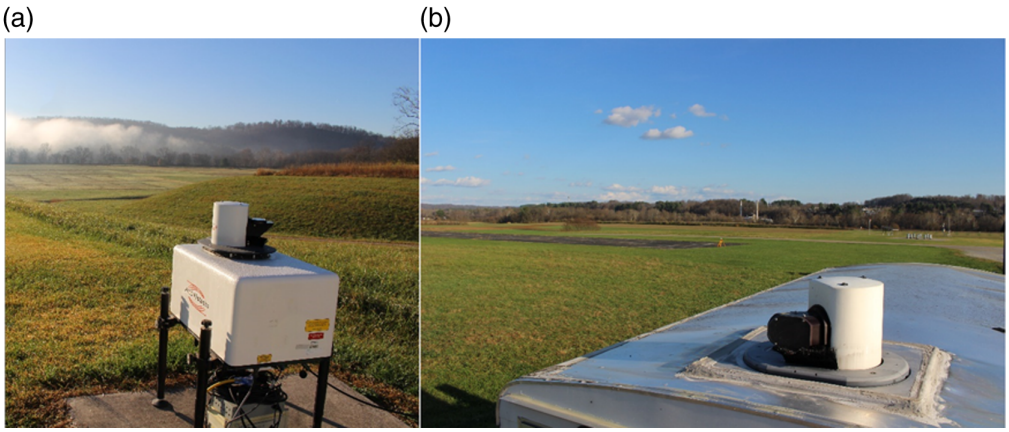

Fig. 2 Two scanning Doppler Lidars used in this study. One lidar was placed directly on a concrete pad (a), whereas the second lidar was integrated into a cargo trailer with beam steering optics protruding from the roof (b).

spatial-temporal comparison with *in situ* instruments to evaluate the feasibility of dual-Doppler for AAM. An experiment was devised in which the two Doppler lidars, a sonic anemometer, and a hovering multi-rotor sUAS all sampled the same volume. The two lidars, sonic anemometer, and sUAS can be seen in Figs. 2–4.

Both lidars were programmed to intersect beams at the reference position, and a sonic anemometer was placed near this intersection. Simultaneously, a UVA-operated sUAS would hover near the sonic anemometer allowing for a comparison of wind measurements from each instrument. Details and results from this comparison are in Sec. 4.2.

To expand the dual-Doppler measurements throughout the airspace above KEAS, both lidars were programmed to intersect at multiple altitudes above the reference position through Range Height Indicator (RHI) scans (Figs. 11 and 12). By intersecting lidar beams at multiple altitudes above the reference position, wind speed and direction could be measured along a "Virtual Tower" on the KEAS runway (Fig. 15). Although both lidars were performing RHI scans, the UVA sUAS hovered at altitudes near the beam intersections and measured wind speed and direction. An analysis of the recorded data is presented in Sec. 4.3.1.

Fig. 3 Pictures taken near reference position. The sonic anemometer marked "A" is in the foreground at the reference position. Lidar 1 on the image on the left is marked "B," and lidar 2 in the image on the right is marked by "C". Above lidar 2 in the image on the right is the UVA-operated sUAS marked by "D."

Fig. 4 Quadrotor for Wind Estimation Research.

3 Equipment

3.1 Doppler Wind Lidars

During this campaign, two Doppler wind lidar units were used to sample winds in the ABL. Both lidar units are weatherproof and temperature-controlled with class 1 M eye-safe output. Both lidars emit wavelengths of 1.548 μm, and their laser pulse energies are 100 μJ with pulse widths of 150 ns and pulse rates of 15 kHz. Both units are capable of upper hemispherical step-stare scanning. The outgoing lidar beams interact with aerosols acting as a tracer for wind flow in the ABL. The movement of aerosols in the ABL causes a Doppler shift in the backscatter received by the lidar unit which is proportional to the wind velocity along the lidar's line of sight (LOS). Both lidars have a LOS velocity resolution of 0.038 m/s. With differences in their software control features, lidar 1 has a 3-m range resolution, whereas lidar 2 has a range resolution of 18 m.

3.2 Sonic Anemometer

A Gill GMX541 compact weather station was mounted at the reference position coordinates. The compact weather station was installed at a height of 2.5 m above the KEAS runway. The compact weather station measures temperature, humidity, pressure, precipitation, solar radiation, wind speed, and direction. The sonic anemometer on the instrument measures wind speed and direction with a 1 Hz sampling rate. The measured windspeed and direction have a respective resolution of 0.01 m/s and 1 deg and an accuracy of $\pm 3\%$.

The compact weather station measured winds near (and below) the intersection point of the lidar beams and the hovering position of the sUAS.

3.3 Small Uninhabited Aircraft Systems

Among the sUAS in operation during this campaign was a custom-built quadcopter (Fig. 6) used for *indirect wind estimation*—i.e., inferring three-dimensional wind velocity without the use of dedicated sensors such as an anemometer.

Indirect wind estimation is the informed combination of standard navigational sensors [e.g., accelerometer, gyroscope, magnetometer, and Global Navigation Satellite System (GNSS)] with a flight dynamic model (i.e., a set of differential equations that model vehicle motion) to obtain wind velocity from methods described in Refs. 22–24 and 34. The quadrotor was built from a Da-Jiang Innovations FlameWheel F450 frame and was equipped with a Cubepilot Cube Orange flight computer running PX4 firmware for navigation and control purposes. The sensor suite included a real-time kinematics-capable GNSS receiver enabling up to 1 cm accurate positioning, two magnetometers (one internal and one in the GNSS puck), triple-redundant accelerometers, and a gyroscope.

During this campaign, another multi-rotor sUAS was used. This sUAS was a commercial off-the-shelf drone and was operated by a UVA pilot during the campaign. This sUAS weighs 0.25 kg and has a diagonal size of 213 mm. The sUAS flight log data extracted from this drone includes attitude data, accelerometer data, and global positioning system (GPS) data. This data were then used to calculate the horizontal wind speed following the indirect wind estimation methodology described in Refs. 33 and 34.

4 Data Retrieval Methods and Results

4.1 Velocity Azimuth Display Scans

The first experiment during this campaign was to collect wind profiles with a single lidar near the KEAS runway. Wind profiling via VAD scans measures winds aloft with a single lidar. Illustrated in Fig. 5, a VAD scan consists of the lidar beam scanning a conical volume of the atmosphere above the unit. The lidar beam steering optics are directed to a combination of elevation and azimuthal angles which orient the beam to the required positions to complete a VAD scan. Each VAD yields the data required to calculate a wind profile above the lidar. The programmed VAD scan takes ~30 s to complete. During this 30-s period, it is assumed that the flow field is homogenous, and the vertical wind speed is zero when calculating the wind profile. As the altitude increases, the cross-sectional area of the scanned conical volume increases which averages the wind field over a larger area, hence decreasing resolution. VAD scans from a single lidar offer less resolution than the dual-Doppler techniques discussed later but may still be of use at future vertiports for providing measurements of winds aloft.

Lidar 1 was programmed to complete VAD scans every 2 min with an elevation angle $\theta = 45$ deg and to rotate with an azimuthal angle $\phi = 60$ deg to six positions, as seen in Fig. 5.

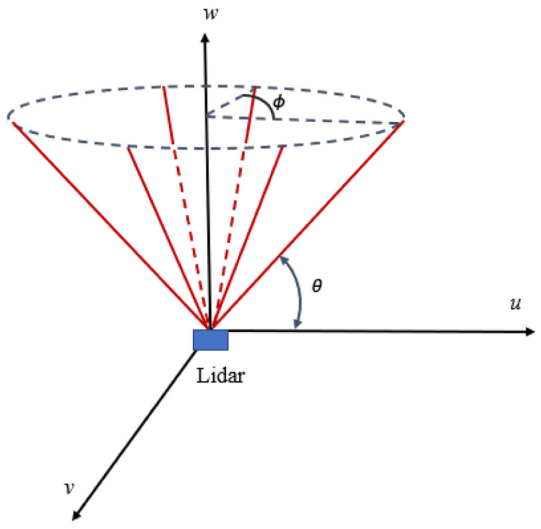

Fig. 5 Illustration of six-position VAD scan.

The range resolved radial wind velocity v_r is measured at six different beam orientations for one VAD scan cycle, with u and v being the easting and northing wind velocity components, respectively, and w being the vertical wind velocity component. By measuring the time of flight between the outgoing pulses of the lidar and the backscatter signal received by the lidar, the data are resolved by range. This process yields LOS velocities throughout the beam path. The lidar unit's signal processor discretizes the Doppler-shifted backscatter throughout the effective range of the lidar into range gates. Each range gate has a set length (range gate length) which is 18 m for each lidar. The measurement from each lidar unit produces data that records an LOS velocity at the center of each range gate by averaging the LOS velocities throughout the respective range gate's gate length. Lidar 1 had overlapping range gates, yielding radial wind velocity measurements every 3 m.

The equations describing the radial velocities of VAD scans from Refs. 20 and 21 are described below.

Combining the equations for the radial velocities of a VAD scan gives a set of linear equations. In matrix form this set of linear equations is,

$$\mathbf{A}\boldsymbol{v} = \boldsymbol{v_r}, \tag{1}$$

where $\boldsymbol{v}$ is the wind vector,

$$\boldsymbol{v} = \begin{bmatrix} u \\ v \\ w \end{bmatrix}. \tag{2}$$

Moreover, $\boldsymbol{V_r}$ is a vector composed of radial velocities measured from the VAD scan.

$$\boldsymbol{v_r} = \begin{bmatrix} V_{r1} \\ V_{r2} \\ V_{r3} \\ V_{r4} \\ V_{r5} \\ V_{r6} \end{bmatrix}. \tag{3}$$

The matrix $\mathbf{A}$ below describes the relationship between the radial velocities $\boldsymbol{V_r}$ and the wind vector $\boldsymbol{v}$.

$$\mathbf{A} = \begin{bmatrix} \sin(\phi_1)\sin(\theta) & \cos(\phi_1)\cos(\theta) & \cos(\theta) \\ \sin(\phi_2)\sin(\theta) & \cos(\phi_2)\cos(\theta) & \cos(\theta) \\ \sin(\phi_3)\sin(\theta) & \cos(\phi_3)\cos(\theta) & \cos(\theta) \\ \sin(\phi_4)\sin(\theta) & \cos(\phi_4)\cos(\theta) & \cos(\theta) \\ \sin(\phi_5)\sin(\theta) & \cos(\phi_5)\cos(\theta) & \cos(\theta) \\ \sin(\phi_6)\sin(\theta) & \cos(\phi_6)\cos(\theta) & \cos(\theta) \end{bmatrix}. \tag{4}$$

This system of equations can be solved with a least squares algorithm which would yield the three components of the wind vector.

Lidar 1 was programmed to perform VAD scans from September 13 through November 7.

On September 22, a Virginia Tech rotor-wing sUAS performed flight tests. The VAD data for September 22 is shown in Fig. 6.

With lidar 1 programmed to perform a VAD scan every 2 min, a range-resolved horizontal wind speed and direction value is plotted versus time in coordinated universal time (UTC). These plots offer visualization of dynamics within the ABL and the relevance of wind effects for low-level flight. For example, Fig. 6(b) shows from 00:00 to 11:00 UTC that the wind speed is near zero up to about 200-m height, rapidly increasing to 7.5 m/s above 200 m. If a ground-based anemometer were the only sensor available, then the near-zero wind speeds at ground level may give a pilot a false assumption that the wind speeds at a slightly higher altitude were also near zero. Another wind feature can be seen from 03:00 to 09:30 UTC with wind speeds of 15 to 20 m/s above 500-m altitude. After sunrise, the wind speed increases at low altitudes and

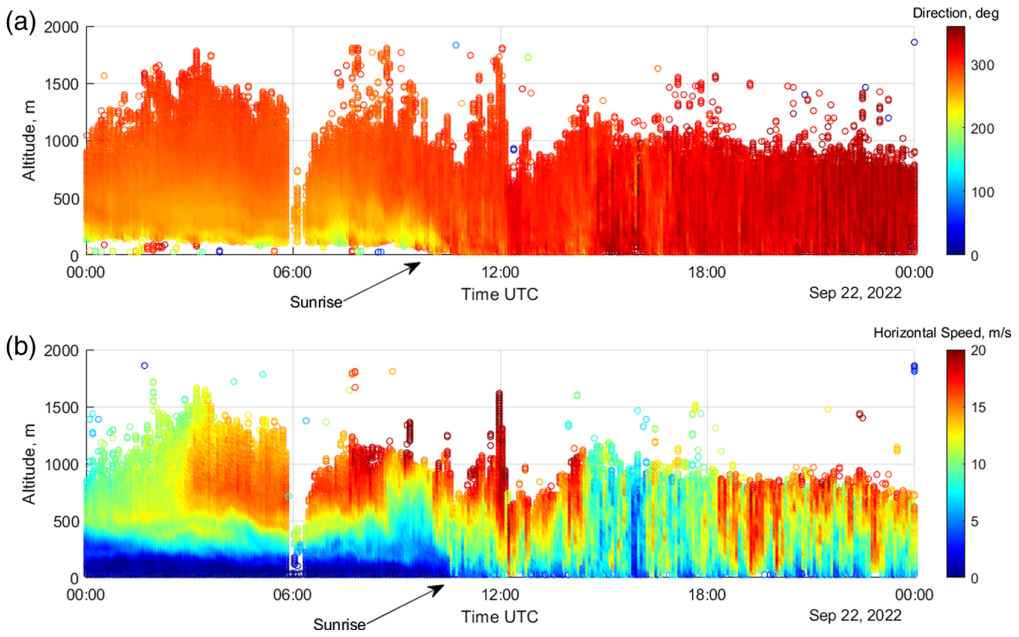

Fig. 6 September 22, 2022, VAD-derived wind data for (a) direction and (b) horizontal speed. Time in UTC.

becomes gustier in the convective boundary layer at all altitudes up to the 1000-m altitude range capability of the lidar on this day.

4.2 Indirect Wind Estimation from Quadrotor Motion

When a single lidar profiles wind using VAD scans, homogeneity of the wind vector throughout both the scanned volume and the duration of the scan is assumed. The single wind lidar is therefore unable to measure wind variations at time scales shorter than the scan duration. To investigate wind effects at these shorter time scales, a quadcopter hovered at various altitudes within the scanning volume of the lidar unit.

The quadcopter obtains three-dimensional wind estimates at high temporal and spatial resolutions only limited by the vehicle's inertia/sampling rate and the GNSS positioning accuracy, respectively. For the experiment described here, this wind measurement is accomplished using a linear, time-invariant (LTI) flight dynamic model as part of a square-root information filter (SRIF) that estimates the extended systems state. *Extended system state* means the vector of variables that describe the vehicle's position, attitude, air-relative velocity, angular velocity, and wind velocity (the *extension* to the vehicle's state of motion). The state vector, $\boldsymbol{x}$, satisfies the LTI dynamics

$$\frac{d\boldsymbol{x}}{dt} = \mathbf{A}x(t) + \mathbf{B}\boldsymbol{u}(t) + \mathbf{D}\tilde{v}(t), \tag{5}$$

where $\boldsymbol{u}$ is the vector of control inputs (e.g., motor speeds) and $\tilde{v}$ is continuous-time zero-mean Gaussian white noise with power spectral density Q. This model (namely the $\mathbf{A}$, $\mathbf{B}$, and $\mathbf{D}$ matrices) was identified from flight test data using standard aircraft system identification techniques from Refs. 25 and 26. The output of the system, y, is discretely sampled and is modeled as

$$y(k) = Cx(t_k) + v(k), \tag{6}$$

where t_k is the time of the k'th measurement and v is the measurement noise with each $v(k)$ independently sampled from a Gaussian distribution with mean zero and covariance R. The SRIF yields state estimates $\hat{x}(t_k) = E\{x(t_k)|\mathcal{Z}^k\}$ where $\mathcal{Z}^k$ is the set of measurements up to sample number k and $E\{\cdot \mid \cdot\}$ is the conditional expectation. This estimate, which includes the wind velocity estimate $\hat{\boldsymbol{w}}$, is obtained in a numerically efficient and stable manner—the main advantage of the SRIF over the Kalman filter described in Ref. 27. An example of the indirect wind estimation results is shown in Fig. 7 along with wind lidar measurements. Here, the estimated

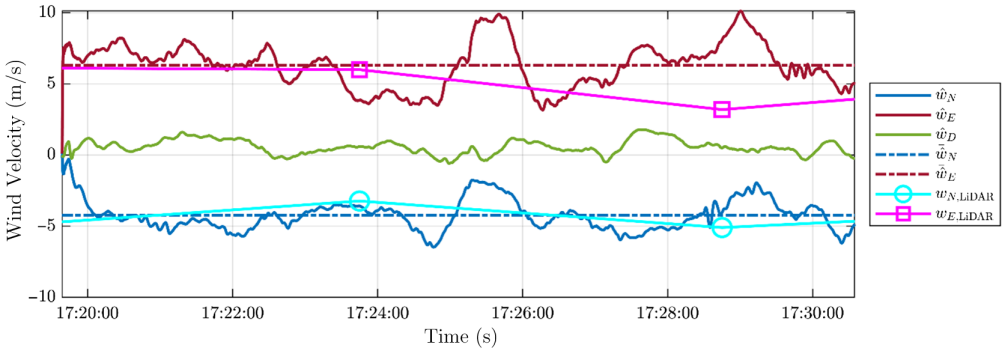

Fig. 7 September 22, 2022, Quadrotor Indirect Wind Estimates using the SRIF and comparison with lidar VAD scan at 122 m.

wind vector, $\hat{\boldsymbol{w}} = [\,\hat{w}_N \quad \hat{w}_E \quad \hat{w}_D\,]^T$, is expressed in a local North-East-Down reference frame. The North and East direction wind measurements obtained from the lidar VAD scans are denoted $w_{N,\mathrm{LiDAR}}$ and $w_{E,\mathrm{LiDAR}}$, respectively. The dashed lines in Fig. 7 show the average value of the respective wind estimate component over the course of the maneuver.

Comparing the lidar with airborne *in situ* wind measurements shows close agreement of the lidar with the time average of the *in situ* sensor, providing a validation of the results from each of the two measurement systems. However, the relatively long-timescale integration of the lidar, coupled with a sampling area of ~325 m^2 should be noted. The airborne *in situ* sensor is sampling the wind at a much higher rate and showing fine-scale variations at the drone's specific location. In related research, the high sample rate of rotorcraft-based measurements similar to those used in the data of Fig. 7 has been evaluated with encouraging results for the capability of measuring turbulence (Ref. 28).

With AAM envisioning the operation of low-flying aircraft in urban environments, the spatial-temporal resolution of the wind field measured from the VAD scans may not be sufficient. To increase the resolution of wind measurements from lidars, a dual-Doppler approach was taken. This dual-Doppler approach allowed for a direct spatial-temporal comparison between the lidars and *in situ* instrumentation. Details of these experiments are described in the following sections.

4.3 Dual-Doppler, Sonic Anemometer, and sUAS Point Comparison

The advantage and utility of dual-Doppler lidar lies in scanning the lidars' beams to sample a volume. However, dual-Doppler tests were initially conducted without beam scanning to measure winds at a beam-intersection point for sensor intercomparison. A direct spatial-temporal comparison among lidars, sUAS, and a sonic anemometer was performed to compare the dual-Doppler wind vector measurements with *in situ* instruments. Both lidar beams were oriented to intersect directly above the sonic anemometer located at the reference position. Simultaneously, the UVA-operated sUAS hovered in proximity to the reference position, allowing for a direct spatial-temporal comparison of the horizontal wind vectors in the ABL.

The positioning of each lidar was predetermined such that the intersection angle of the lidar beams above the reference position was near perpendicular and for each lidar unit to have access to power throughout the duration of the field deployment. To ensure each lidar was pointing in the intended direction, the pitch and roll and bearing of each unit were optimized. Adjustment knobs and referencing an internal inertial measurement unit allowed for accurate adjustment of each unit's pitch and roll. The bearing was calculated using the latitude and longitude of the lidars and nearby references to which the lidars were aligned. This allowed for accurate azimuthal angle input and reading such that when the lidar would point directly North, the azimuthal angle was at 0 deg, and when it was pointed East, it was at 90 deg.

Each lidar's radial wind velocity v_{ri} was measured from its respective orientation. From Ref. 10, the mathematical description is

$$v_{ri} = u \sin\phi_i \cos\theta_i + v \cos\phi_i \cos\theta_i + w \sin\theta_i \tag{7}$$

where $\boldsymbol{i}$ denotes which lidar unit, $\boldsymbol{\theta_i}$ is the elevation angle for the respective lidar, and $\boldsymbol{\phi_i}$ is the azimuthal angle for the respective lidar.

Assuming the vertical wind component $\boldsymbol{w}$ to average out to zero in the in the ABL, only the easting and northing components $\boldsymbol{u}$ and $\boldsymbol{v}$ are taken into account for each lidar radial wind velocity $\hat{\boldsymbol{v}}_{\boldsymbol{ri}}$.

$$\hat{\boldsymbol{v}}_{\boldsymbol{ri}} = u \sin \phi_i \cos \theta_i + v \cos \phi_i \cos \theta_i. \tag{8}$$

From Eq. (6), the horizontal wind components u and v can be solved.

$$u = (\hat{\boldsymbol{v}}_{\boldsymbol{r1}} \cos \phi_2 \cos \theta_2 - \hat{\boldsymbol{v}}_{\boldsymbol{r2}} \cos \phi_1 \cos \theta_1)/\Delta, \tag{9}$$

$$v = (\hat{\boldsymbol{v}}_{\boldsymbol{r2}} \sin \phi_1 \cos \theta_1 - \hat{\boldsymbol{v}}_{\boldsymbol{r1}} \sin \phi_2 \cos \theta_2)/\Delta. \tag{10}$$

For simplification Δ is,

$$\Delta = \cos \theta_1 \cos \theta_2 (\sin \phi_1 \cos \phi_2 - \sin \phi_2 \cos \phi_1). \tag{11}$$

To intersect lidar beams at the reference position, elevation and azimuthal angles were referenced to a hard-target marker pole temporarily placed at the end of the runway. The beam from each lidar was adjusted to strike the pole position and height by visually observing the incidence of the laser spot on the pole. This visual observation was made with an infrared viewer that can see the 1550-nm wavelength of the laser beam. Surveying the location of the pole and the locations of the lidars allowed calibration to true north, as summarized by the azimuth entries in Table 1. Elevation settings to strike the pole reference height are also listed in Table 1, with the different values among the two lidars showing that the terrain is not flat. Elevation settings of the lidar beams can be influenced by the degree of level (the "roll" and "pitch" of the lidar units), so each unit was leveled as close as possible to zero roll and pitch. A tilt sensor internal to the lidar units makes this leveling possible.

With the lidar intersection at the reference position confirmed, the correct range gates for each lidar were selected. The range gate length for both lidars is 18 m. Lidar 1 had an overlapping range gate feature which lidar 2 did not. Lidar 1 therefore had measurements every 3 m, whereas lidar 2 yielded measurements every 18 m. The LOS velocity for each range gate is averaged over the gate length, and this averaged LOS velocity $\hat{v}_{ri}$ is located at the center of the range gate. Using a laser range finder, the distance from lidar 1 to the reference point was measured to be 62.15 m and the distance from lidar 2 to the reference position was 55.9 m. The range gate closest to the reference position for each lidar was selected. For lidar 1, range gate 20 was chosen because of its corresponding distance of 61.5 m, and for lidar 2, range gate 3 was chosen because of its corresponding distance of 63.0 m. These distances are centered at the respective gate lengths ensuring the sampled wind for both lidars overlaps at the reference point. Each lidars' measured $\hat{v}_{ri}$ is calculated from averaged velocity measurements throughout their respective range gates.

Using Eqs. (7) and (8), the u and v components are calculated from the measured LOS velocities from the lidars, whereas the sUAS u and v components were calculated by methods described in Refs. 24–27.

The dual-Doppler wind measurements were then compared with the sonic anemometer and sUAS hovering at the reference position. The results for the ~20- min comparison are shown in Fig. 8.

Data from the three instruments follow similar trends throughout the duration of this comparison (Fig. 8). The sonic anemometer and sUAS record larger magnitudes than the dual-Doppler lidar for velocity along the easting component u [Fig. 8(a)]. For the northing component

Table 1 Azimuth and elevation angles for each lidar unit.

Angles	Lidar 1	Lidar 2
Azimuth ϕ_i	3.85 deg	110.66 deg
Elevation θ_i	1.56 deg	–0.39 deg

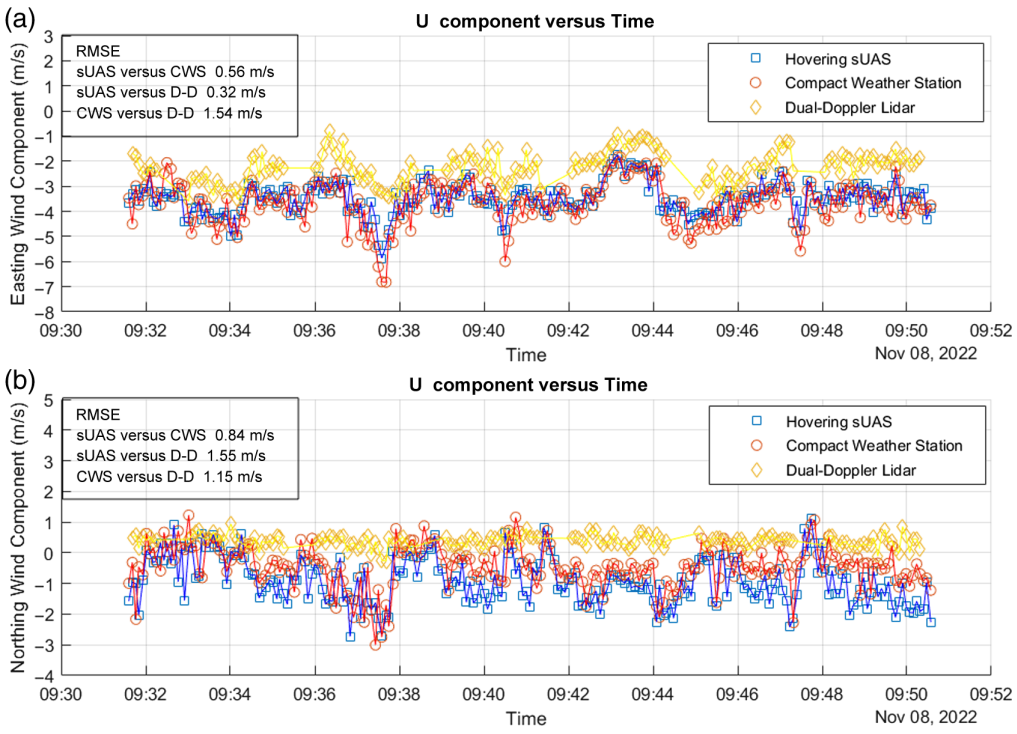

Fig. 8 Easting component u (a) and Northing component v (b) measured at the reference position by the sUAS, sonic anemometer, and dual-Doppler lidar and plotted with different symbols and colors. RMSE values were calculated and appear at the top left of plots (a) and (b).

v [Fig. 8(b)], the velocities are closer to 0 m/s with the sonic anemometer and sUAS mostly recording larger velocity magnitudes than the dual-Doppler lidar measurements.

The u and v measurements are used to calculate the horizontal wind speed and direction at the reference position on the KEAS runway using equations,

$$W_s = \sqrt{u^2 + v^2}, \tag{12}$$

and,

$$W_D = 180 + \frac{180}{\pi} \operatorname{atan2}(u, v), \tag{13}$$

The calculated horizontal wind speed and direction at the reference position for all instrumentation and root mean square error (RMSE) values are shown in (Fig. 9), and the RMSE values are displayed in the top left of plots **(a)** and **(b)**.

The three instruments follow similar trends in horizontal wind speed [Fig. 9(a)], with the lidar reporting a lower wind speed than a sonic anemometer, as also been reported in Ref. 10. Additional insight is offered in this study by adding another type of *in situ* sensor in the form of the hovering sUAS. The close agreement of the two *in situ* sensors, compared with the offset of the lidar results, suggests that the cause of the offset between the two sensor types is caused by the difference in point versus volume-averaged sampling. In other words, it is hypothesized that the cylindrical laser beam takes an ensemble average of Doppler backscatter spectra from over the length of a range bin and the diameter of the outgoing beam. This volume average may tend to reduce the measured speed in this situation.

The direction calculated from the *in situ* sensors yielded similar directional results [Fig. 9(b)]. All three sensors are in general agreement on wind direction, with only small offsets between the sensors. For example, while the sonic anemometer and hovering sUAS agreed closely in wind speed, their direction measurements showed a constant small bias. The dual-Doppler measurements also showed a bias from each of the two *in situ* sensors.

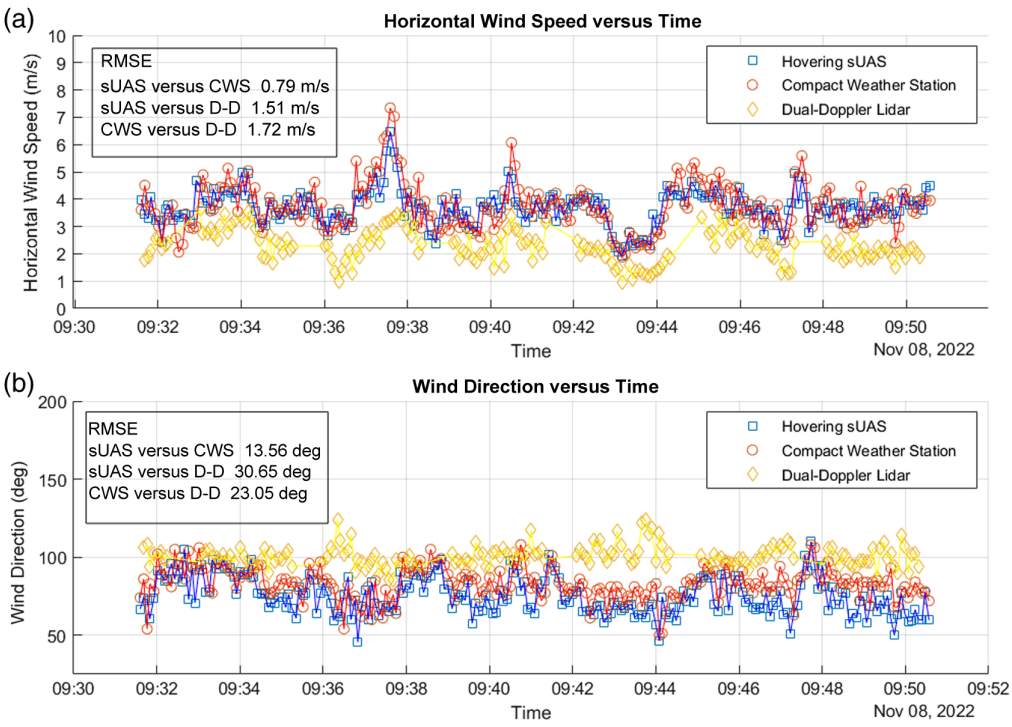

Fig. 9 Horizontal wind speed (a) and the direction (b) measured at the reference position by the sUAS, sonic anemometer, and dual-Doppler lidar and plotted with different symbols and colors. RMSE values were calculated and appear at the top left of plots (a) and (b).

This wind vector comparison was performed at a fixed altitude above the runway. In the following section, a comparison of wind vectors at various altitudes could be performed using a different lidar scan pattern.

4.4 Dual-Doppler RHI Intersection

Following the point stare comparison in Sec. 4.2, the next step was to compare winds at multiple altitudes. To do this both lidars were programmed to perform intersecting RHI scans.

Throughout the duration of the RHI scan, the lidar beam's azimuthal angle ϕ, is fixed while it cycles through discrete elevation angles θ, as illustrated in Fig. 10. This scan provides range-resolved radial velocity $\hat{v}_{ri}$ measurements via Doppler-shifted backscatter from aerosols in the ABL.

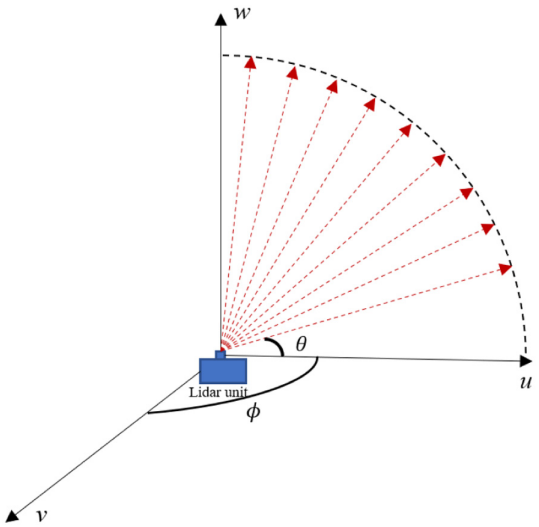

Fig. 10 Illustration of RHI scan.

Fig. 11 Image and Illustration of KEAS Virtual Tower experimental setup where "A" is the reference position, "B" is Lidar 1, and "C" is Lidar 2.

The intersection of two RHI scans would allow for wind speed and direction measurements similar to those measured in Sec. 4.2, but throughout a vertical column. Both lidars were programmed to perform RHI scans that would intersect above the reference position. At the azimuthal intersection of the RHI's, each lidar was programmed with respective elevation angles θ_i to intersect at predetermined altitudes above the reference position as illustrated in Fig. 11.

These intersections at defined altitudes allow for wind speed and direction measurements throughout a vertical column or a "virtual tower."

With both lidars performing RHI scans, a sUAS would hover and record wind speed and direction measurements at select altitudes, performing a vertical wind profile in proximity to the virtual tower. A pair of RHI scans during the sUAS flight test are plotted below in Figs. 12 and 13.

Figures 12 and 13 are radial scatter plots with radial distances and elevation angles θ_i for each lidar unit. The first 45 m of lidar data is filtered out. The higher density of data in Fig. 12 is due to lidar 1 having the overlap function enabled. For each lidar's elevation angle θ_i, the range gates nearest to the virtual towers for both lidars were selected to calculate the horizontal wind vectors. To calculate the horizontal component of each lidar's LOS velocity, Eqs. (7)–(11) were used.

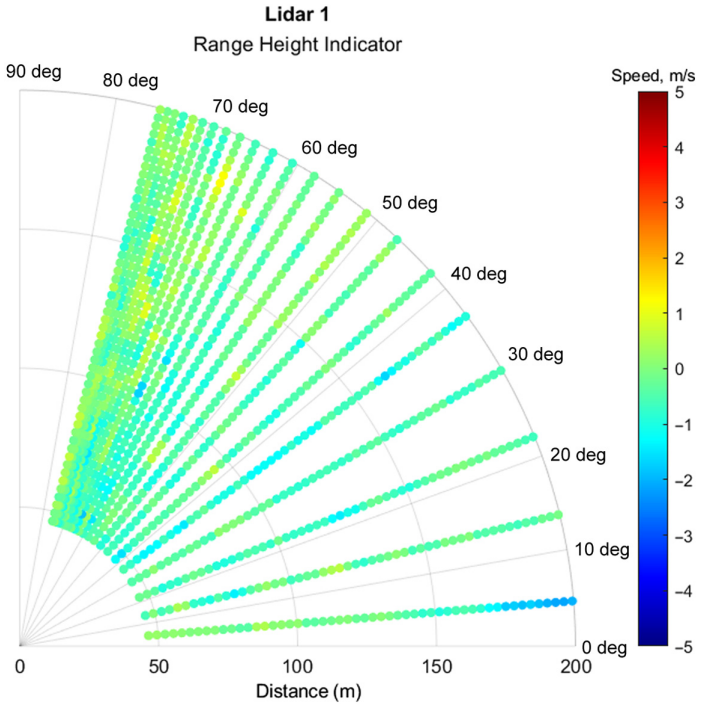

Fig. 12 RHI plot for lidar 1 during sUAS flight.

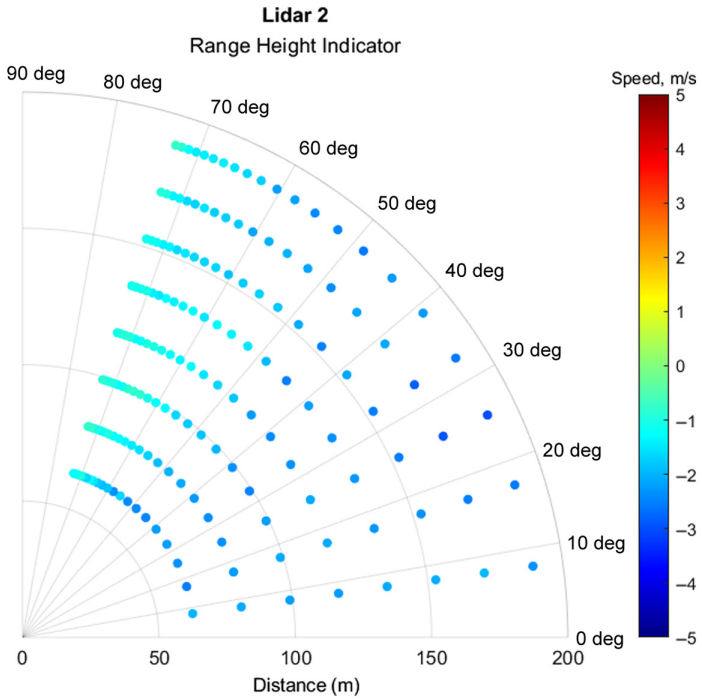

Fig. 13 RHI plot for lidar 2 during sUAS flight.

There was a delay of ∼4 s between lidars 1 and 2 beginning RHI scans. Each lidar's RHI scan duration was ∼30 s, and each would repeat scans upon completion. Each RHI pair would create a virtual tower. Simultaneous with the RHI scans, the UVA-operated multi-rotor sUAS performed a vertical wind profile near the virtual tower measuring horizontal winds. The vertical profile flight lasted 5 min during which the sUAS hovered for at least 10 s at increments of 10 m above ground level (AGL) with the sUAS's final hover at 120 m AGL. The 120-m AGL flight ceiling was chosen to remain under the 400-ft AGL Federal Aviation Administration limit.

A comparison between dual-Doppler and sUAS-derived measurements at different altitudes was now possible. During the 5-min sUAS profile, the lidars would scan seven virtual towers. Windspeed and direction measurements from the virtual towers and the sUAS are plotted in Fig. 14.

Wind speed and direction measurements from the dual-Doppler virtual tower range from 10 to 210 m AGL at 10-m increments and the UVA-operated sUAS measured wind speed and direction at 10-m increments from 10 to 120 m AGL. The sUAS flight occurred over a 5-min period with the lidars performing continuous RHI scans throughout the duration of the flight. A comparison between the two measurement techniques assumes constant winds over a 5-min period. Similar to Fig. 9, for the non-scanning lidar experiment, the lidar reports a lower wind speed measurement at all altitudes by 1 to 2 m/s. In addition, in agreement with the findings of Fig. 9, the lidar reports a difference of 10 to 20 deg in wind direction compared with the sUAS measurements.

4.5 Dual-Doppler, Virtual Tower Visualization

Although Fig. 15 is useful for conveying quantitative wind vector information, an alternate visualization tool was developed to display dual-Doppler lidar virtual towers in a qualitative format. This technique allows for better visualization of the wind field measured by the virtual tower. This tool displays the relative positions of lidars and the virtual tower created from intersecting their RHI scans in a virtual 3D space.

Along the virtual tower are arrows representing the measured wind vectors from the intersection of RHI scans. The LOS wind velocity measured at the virtual tower along with the azimuthal and elevation angle from each lidar is used to calculate each wind vector along the tower using Eqs. (7)–(11). These arrows point in the direction of wind, and their length and color represent measured wind speed. Together, the color and direction of the arrows display the wind

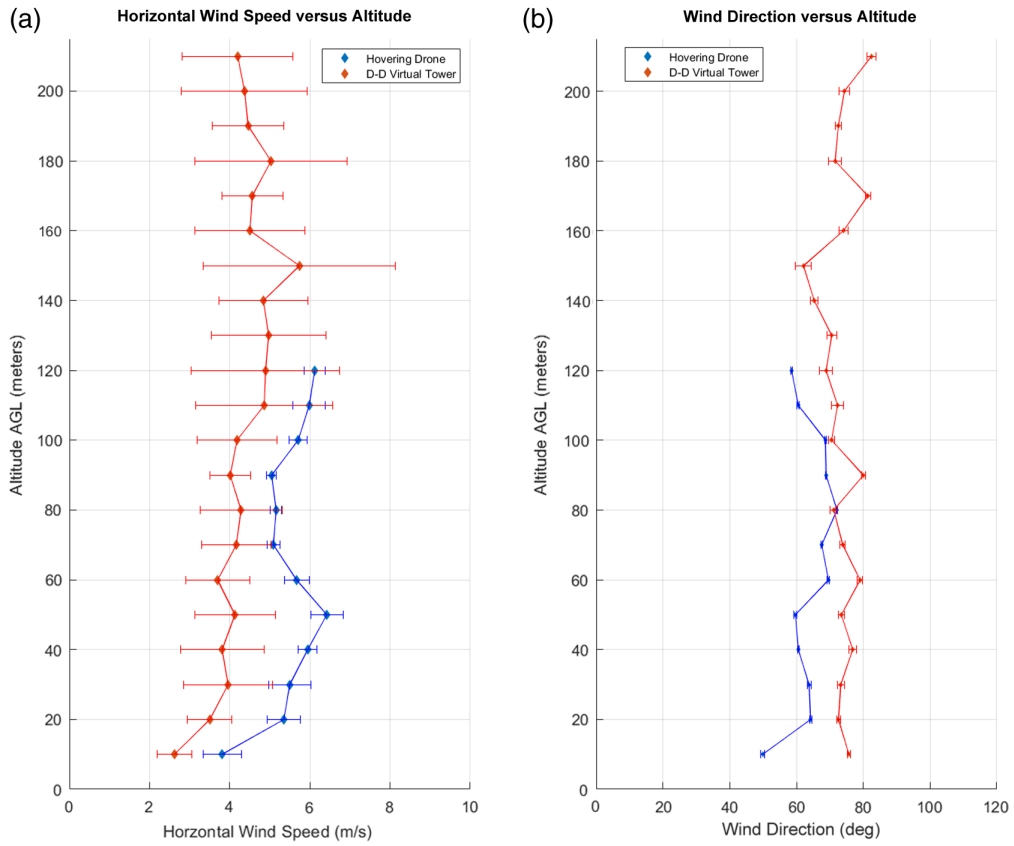

Fig. 14 Comparison between dual-Doppler and sUAS for (a) horizontal wind speed and (b) wind direction versus altitude. The diamonds are positioned at the mean recorded horizontal wind speed and direction, and the error bars represent the standard deviation.

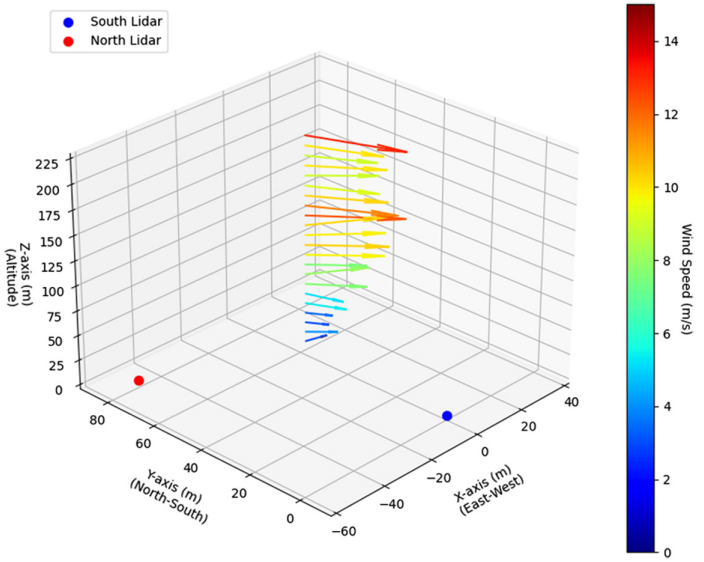

Fig. 15 Virtual tower visualization.

vectors along the virtual tower. Future campaigns in more complex environments could add the buildings and obstacles at the test site within this 3D model, helping to visualize the flow field around the buildings measured by the lidars. A 3D visualization of the flow field would help the AAM mission better understand how to travel through similar environments.

In Fig. 15, the positioning of the two wind lidars and the virtual tower is representative of the deployment at KEAS. The positioning was recorded through GPS and distances via a laser range finder. The two horizontal axes represent the North and East direction in meters, and the vertical axis represents the altitude AGL in meters. The maximum altitude and spacing between vectors are adjustable to the application. In this example, vectors are spaced every 10 m up to 210 m AGL. Ensuring spatial intersection of lidar beams at discrete altitudes and synchronizing both lidar units to sample the volume at those altitudes yields spatial-temporally resolved wind vector measurements from near-ground level to 100 m of AGL, meeting AAM wind sensing requirements.

5 Summary and Conclusions

The campaign at KEAS evaluated the use of Doppler lidar for meeting the anticipated needs of AAM for wind sensing. A field deployment spanning 3 months provided encouraging results, with commercial wind lidar units providing reliable automated operation. Lidar results were compared with data from other instruments, including a ground-based sonic anemometer and sUAS.

A single VAD scanning wind lidar is useful for providing wind profiles to measure wind vector variation with height and occurrences of shear. The availability of such profiles in the ABL may be critical for vertiport operations. Although lidar wind profiling measurements have been validated in many prior studies by other instruments, including balloon sondes, drop sondes, and sodar. Wind lidar measurements were validated by comparison with airborne *in situ* measurements provided by sUAS.

Although a VAD scanning single lidar is useful for characterizing winds in the ABL, localized effects require better spatial and temporal resolution. These localized effects can include turbulence created by buildings, terrain-induced effects, and aircraft wake turbulence. The latter issue may become a limiting factor to safety and efficiency if many vehicles are cycled through a vertiport. The size of the turbulent rolls or eddies that can affect vehicles is likely to be on the order of 10 m, and the test shows that such spatial resolution can be achieved with the dual-Doppler technique.

Wind vector measurements were validated using the dual-Doppler technique against other sensors throughout several tests. One such test was to intersect a dual-Doppler measurement at the same location as two *in situ* sensors, including a ground-based sonic anemometer and multi-rotor sUAS's capable of measuring winds. All three sensors agreed in measurements to be within 1 to 2 m/s of wind speed and 20 to 30 deg of wind direction. As reported in earlier dual-Doppler studies, this study also found that the dual-Doppler lidar wind measurements were consistently less than *in situ* sensors by about 1 m/s. This constant offset is hypothesized to be attributed to the difference between the lidars' volumetric sensing vs the *in situ* point sensing of wind, but this needs further investigation.

The dual-Doppler technique was further tested by setting up a "virtual tower" composed of intersecting RHI scans from each lidar. Wind measurements up to 210-m height in 10-m increments of height were performed. These wind measurements compared well between the dual-Doppler lidar and the *in situ* multi-rotor sUAS. Both the lidar and *in situ* sensors showed the same trend with altitude. As was found with the fixed-point measurement, the dual-Doppler lidar reported the wind speed about 1 m/s lower than the *in situ* sensor, which is attributed to volumetric versus point sensing of wind.

The results from the wind lidar tests are encouraging toward fulfilling wind measurement needs, and future work is planned toward AAM interests. The intention is to set up multiple virtual towers to study wind effects in the lee of a large building structure to simulate conditions of a vertiport in an urban setting. Several virtual towers placed downwind of the building could allow measurement of turbulent flow around the building, as well as visualization using the techniques developed in this paper. Another potential subject of study is wake vortex turbulence at vertiports, both to better understand the complex turbulence created by a new class of vertical take-off and landing aircraft and as a potential monitoring system for vertiports. The initial study reported here showed several lessons in implementing dual-Doppler lidar for these future applications: intersecting lidar beams at the desired altitudes, synchronization as closely as possible, and accurate geolocation for each lidar.

Disclosures

The authors declare there are no known financial, commercial, or other conflicts of interest that could have influenced the objectivity of this research and the writing of this paper.

Code and Data Availability

Data presented in this article is available upon request with permission from the organizations involved in this study.

Acknowledgments

This study was made possible by the NASA Aeronautics Research Mission Directorate's Convergent Aeronautics Solutions project. The authors would like to thank the members of the Nonlinear Systems Laboratory and the Kentland Experimental Aerial Systems facility coordinator, Brooks Saville, for supporting the lidar and UAS operations throughout this campaign.[35]

References

1. J. Banke, "Advanced air mobility mission," Nasa.gov (28 December 2023). https://www.nasa.gov/mission/aam/ (accessed 14 March 2024).
2. Federal Aviation Administration, "UTM Concept of Operations Version 2.0 (UTM ConOps v2.0)," https://www.faa.gov/researchdevelopment/trafficmanagement/utm-concept-operations-version-20-utm-conops-v20.
3. J. F. Barlow, "Progress in observing and modelling the urban boundary layer," *Urban Clim.* **10**(Part 2), 216–240 (2014).
4. I. Eliasson et al., "Wind fields and turbulence statistics in an urban street canyon," *Atmos. Environ.* **40**(1), 1–16 (2006).
5. P. Brockman et al., "Coherent pulsed Lidar sensing of wake vortex position and strength, winds and turbulence in the terminal area," in *Tenth Biennial Coherent Laser Radar Technol. and Appl. Conf.* (1999).
6. G. Deskos, A. del Carre, and R. Palacios, "Assessment of low-altitude atmospheric turbulence models for aircraft aeroelasticity," *J. Fluids Struct.* **95**, 102981 (2020).
7. G. J. Koch and B.W. Barnes, "Wind event warning system," US Patent 10,067,236 (2018).
8. G. J. Koch et al., "Three-dimensional wind profiling of offshore wind energy areas with airborne Doppler lidar," *J. Appl. Remote Sens.* **8**(1), 083662 (2014).
9. C. G. Collier et al., "Dual-Doppler Lidar measurements for improving dispersion models," *Bull. Amer. Meteor. Soc.* **86**, 825–838 (2005).
10. R. K. Newsom et al., "Turbine-scale wind field measurements using dual-Doppler lidar," *Wind Energy* **18**, 219–235 (2015).
11. D. A. Smith et al., "Wind lidar evaluation at the Danish wind test site in Høvsøre," *Wind Energy* **9**, 87–93 (2006).
12. J. P. Goit, A. Yamaguchi, and T. Ishihara, "Measurement and prediction of wind fields at an offshore site by scanning Doppler LiDAR and WRF," *Atmosphere* **11**(5), 442 (2020).
13. Y. L. Pichugina et al., "Doppler Lidar–based wind-profile measurement system for offshore wind-energy and other marine boundary layer applications," *J. Appl. Meteorol. Climatol.* **51**, 327–349 (2012).
14. G. V. Iungo and F. Porté-Agel, "Volumetric Lidar scanning of wind turbine wakes under convective and neutral atmospheric stability regimes," *J. Atmos. Oceanic Technol.* **31**, 2035–2048 (2014).
15. C. Rahlves, F. Beyrich, and S. Raasch, "Scan strategies for wind profiling with Doppler Lidar—an large-eddy simulation (LES)-based evaluation," *Atmos. Meas. Tech.* **15**, 2839–2856 (2022).
16. Y. Wang et al., "Triple Doppler wind LiDAR observations during the mountain terrain atmospheric modeling and observations field campaign," *J. Appl. Remote Sens.* **10**(2), 026015 (2016).
17. N. S. Prasad and A. R. Mylapore, "Three-beam aerosol backscatter correlation LiDAR for wind profiling," *Opt. Eng.* **56**(3), 031222 (2017).
18. N. W. Cherukuru et al., "Instrument configuration for dual-Doppler LiDAR coplanar scans: METCRAX II," *J. Appl. Remote Sens.* **9**(1), 096090 (2015).
19. Z.-H. Yang et al., "Real-time wind field measurements using all-fiber mobile Doppler wind lidar," *Opt. Eng.* **59**(3), 034107 (2020).
20. J. Boventer et al., "Validation of Doppler wind LiDAR measurements with an Uncrewed Aircraft System (UAS) in the daytime atmospheric boundary layer," *J. Atmos. Ocean. Technol.* **41**, 705–723 (2024).
21. T. Willhite, J. Fowler, and A. Medina, "Uninhabited aerial system drop-in balloon-borne radiosonde alternative for lower tropospheric flights," in *AIAA SCITECH 2024 Forum* (2024).
22. J. W. Langelaan, N. Alley, and J. Neidhoefer, "Wind field estimation for small unmanned aerial vehicles," *J. Guidance Control Dyn.* **34**(4), 1016–1030 (2011).

23. J. González-Rocha et al., "Sensing wind from quadrotor motion," *J. Guidance Control Dyn.* **42**(4), 836–852 (2019).
24. K. Gahan, J. W. Hopwood, and C. A. Woolsey, "Wind estimation using an H∞ filter with fixed-wing aircraft flight test results," in *AIAA SCITECH 2023 Forum*, American Institute of Aeronautics and Astronautics (2023).
25. E. A. Morelli and V. Klein, *Aircraft System Identification: Theory and Practice*, 2nd ed., Sunflyte Enterprises, Williamsburg, VA (2016).
26. J. W. Hopwood and C. A. Woolsey, "Robust linear parameter-varying control for safe and effective unstable aircraft system identification," in *AIAA SCITECH 2024 Forum*, American Institute of Aeronautics and Astronautics (2024).
27. G. J. Bierman et al., "Maximum likelihood estimation using square root information filters," in *Amer. Control Conf.*, IEEE (1989).
28. J. Cooper et al., "Intelligent wind estimation for chemical source localization," in *Proc. Vertical Flight Soc. 79th Annu. Forum*, The Vertical Flight Society (2023).
29. J. W. Hopwood and C. A. Woolsey, "Passivity-based wind estimation for aircraft maneuvering in steady and uniform wind fields," in *AIAA SCITECH 2024 Forum* (2024).
30. K. C. Gahan, J. W. Hopwood, and C. A. Woolsey, "Uncertainty in wind estimates, part 1: analysis using generalized polynomial chaos," in *AIAA 2024-2824. AIAA SCITECH 2024 Forum*, January (2024).
31. K. C. Gahan, J. W. Hopwood, and C. A. Woolsey, "Uncertainty in wind estimates, part 2: H∞ filtering using generalized polynomial chaos," in *AIAA 2024-2825. AIAA SCITECH 2024 Forum*, January (2024).
32. J. K. Cooper, S. F. J. De Wekker, and A. J. Bateman, "Atmospheric sampling strategies with UAS swarms," in *AIAA 2024-2823. AIAA SCITECH 2024 Forum*, January (2024).
33. D. Crowe et al., "Two supervised machine learning approaches for wind velocity estimation using multi-rotor copter attitude measurements," *Sensors* **20**, 5638 (2020).
34. R. T. Palomaki et al., "Wind estimation in the lower atmosphere using multirotor aircraft," *J. Atmos. Ocean. Technol.* **34**, 1183–1191 (2017).
35. T. Willhite and J. D. Jacob, "Inter-comparison of ground and aerial observation systems for urban advanced air mobility wind field campaigns," in *AIAA 2023-2240. AIAA SCITECH 2023 Forum*, January (2023).

Adam Medina is a student trainee in the Remote Sensing Branch at NASA Langley Research Center. He is pursuing his PhD from the University of Central Florida's College of Optics and Photonics (CREOL). He completed his BS in physics from Florida International University.

Zackary Mitchell is an aerospace engineer at NASA Langley Research Center where he works in the Aeronautics Systems Engineering branch. He completed his BS in both mechanical engineering and aerospace engineering from Oklahoma State University.

Tyler Willhite is an aerospace engineer at NASA Langley Research Center where she works in the Uninhabited Aerial Systems Operations Office. She completed her BS in both mechanical engineering and aerospace engineering from Oklahoma State University.

Jeremy W. Hopwood is an aerospace and ocean engineering PhD candidate in the Nonlinear Systems Laboratory at Virginia Tech. He completed his BS in mechanical engineering at the Central Connecticut State University.

Charvi Pande is a student trainee at NASA Langley researcher and is pursuing her BS in aerospace engineering at North Carolina State University. She has completed rotations in the electromagnetics and sensors branch and the dynamics systems and control branch.

Stephan F. J. de Wekker is a professor in the Department of Environmental Sciences at the University of Virginia. His research interests include boundary-layer meteorology, mountain meteorology, mesoscale modeling, and land-atmosphere interactions. He received his MS from Wageningen University and his PhD from the University of British Columbia in atmospheric science.

Craig Woolsey is a professor in the Department of Aerospace and Ocean Engineering at Virginia Tech and is a co-director of the Nonlinear Systems Laboratory. He received a BME in mechanical engineering from Georgia Tech and his MA and PhD from Princeton. His research interests include dynamics and control on nonlinear systems of atmospheric and ocean vehicles.

Kyle Renshaw is an assistant professor in CREOL, the College of Optics and Photonics at the University of Central Florida, where he holds joint appointments in the Department of Physics

and Electrical and Computer Engineering. He conducts research in materials, components, and technologies for imaging systems, including detector, focal plane, and lens technologies, along with system architectures. He is a member of the OSA, SPIE, and IEEE Photonics.

Grady J. Koch received his BS in electrical engineering in 1991 from Virginia Tech, an MS in electrical engineering in 1995 from the University of Illinois at Urbana-Champaign, and his PhD in electrical engineering in 2001 from Old Dominion University. In 1987, he began work at NASA Langley Research Center as a cooperative education student, taking regular employment there in 1991. His research interests include coherent lidar, differential absorption lidar, solid-state lasers, and diode lasers.